



Photodegradation of cytostatic drugs by g-C₃N₄: Synthesis, properties and performance fitted by selecting the appropriate precursor

Álvaro Pérez-Molina^a, Luisa M. Pastrana-Martínez^a, Sergio Morales-Torres^{a,*}, Francisco J. Maldonado-Hódar^a

^a NanoTech - Nanomaterials and Sustainable Chemical Technologies, Department of Inorganic Chemistry, Faculty of Sciences, University of Granada, Avda. Fuente Nueva,s/n., ES-18071 Granada, Spain

ARTICLE INFO

Keywords:

Carbon nitride
Chemical structure
Precursors
Photocatalysis
5-fluorouracil
Cyclophosphamide

ABSTRACT

Graphitic carbon nitride (g-C₃N₄) was synthesized by a one-step thermal method from different N-rich precursors, namely melamine, dicyandiamide, urea, thiourea and cyanamide. The structure, optical and physico-chemical properties of g-C₃N₄ materials were studied by transmission electron microscopy (TEM), X-ray photoelectron spectroscopy (XPS) and Raman spectroscopy, among others. Both melamine and dicyandiamide provided a less porous structure composed by large flake sheets, whereas urea and thiourea favoured g-C₃N₄ composed by small flat sheets and wrinkles with a larger porosity. The establishment of more condensed g-C₃N₄ networks with a reduced band gap was also evidenced for melamine and dicyandiamide precursors, while urea favoured less condensed melem or melon structures. The photoactivity of the different g-C₃N₄ was assessed for the removal of an aqueous solution containing 5-fluorouracil (5-FU), cyclophosphamide (CP) or a mixture of both cytostatic drugs, under near UV-Vis and solar-LED irradiations. The best performing photocatalysts under near UV-Vis irradiation, were those prepared from melamine ($k_{app} = 14.6 \times 10^{-2} \text{ min}^{-1}$ for 5-FU) and thiourea ($k_{app} = 2.5 \times 10^{-2} \text{ min}^{-1}$ for CP), while urea was the most active under solar-LED irradiation ($k_{app} = 0.183 \times 10^{-2} \text{ min}^{-1}$ for 5-FU). In addition, CP was more resistant to be degraded than 5-FU, and a competitive effect for the generated hydroxyl radicals was evidenced when both pollutant molecules were in the same solution. The photoactivity of g-C₃N₄ materials was justified by the combination of various effects: (i) surface area, (ii) well-connected and condensed g-C₃N₄ structures and (iii) high surface C/N ratios with nitrogen vacancies.

1. Introduction

The number of patients requiring chemotherapy increases every year, resulting in a higher consumption of cytostatic drugs for their treatment. The World Health Organization (WHO) classifies the antineoplastic pharmaceuticals into five subgroups according to their chemical structure and cancer cell inhibition mechanism, i.e., alkylating agents, plant alkaloids, antimetabolites, cytotoxic antibiotics, and other antineoplastic agents [1,2]. 5-Fluorouracil (5-FU) and cyclophosphamide (CP) are cytostatic drugs usually used for the treatment of colorectal cancer and non-Hodgkin's lymphoma, respectively. CP is an alkylating agent that inhibits cell proliferation by electro-nucleophilic interaction with the DNA and/or RNA protein, whereas 5-FU is an antimetabolite preventing somatic cell division [3]. In general, cytostatic drugs are consumed at very low concentrations (ppb), however, they have been detected in water and wastewater of several countries

worldwide, facing a serious risk to human health and wild life due to their mutagenic, genotoxic and teratogenic effects [4,5]. Moreover, 5-FU and CP exhibit a low biodegradability and are not entirely removed by the standard treatments used in the municipal wastewater treatment plants (WWTPs), alternative processes for their removal being demanded [5].

Advanced oxidation processes (AOPs) have demonstrated to be effective for water and wastewater decontamination by the effect of highly reactive and non-selective species such as, hydroxyl radicals (HO•) [6]. Among them, heterogeneous photocatalysis employing semiconductors is one of the most promising AOPs for mineralization of a several organic pollutants, or their degradation into easily biodegradable compounds [7,8]. Benchmark metal oxide-based semiconductors, such as TiO₂ and ZnO, have severe limitations in terms of their active sites, high photo-charge carrier recombination rates and poor visible light absorption [9]. Graphitic carbon nitride (g-C₃N₄) is a

* Corresponding author.

E-mail address: semoto@ugr.es (S. Morales-Torres).

<https://doi.org/10.1016/j.cattod.2023.114068>

Available online 27 February 2023

0920-5861/© 2023 The Authors. Published by Elsevier B.V. This is an open access article under the CC BY-NC-ND license (<http://creativecommons.org/licenses/by-nc-nd/4.0/>).

metal-free polymeric n-type semiconductor that has claimed significant attention as a visible light-driven material, due to its simple synthesis, low cost, abundant precursors, non-toxic composition, high thermal stability, high corrosion resistance, narrow band gap (i.e., 2.7 eV) and both conduction (CB) and valence bands (VB) encompass the reduction and oxidation potentials of water, respectively [10,11]. Generally, g-C₃N₄ possesses different allotropes, such as α -C₃N₄, β -C₃N₄, cubic C₃N₄, pseudo-cubic C₃N₄, graphitic C₃N₄, depending on the distribution of basic repeating units based on s-triazine or tri-s-triazine (referred also as heptazine) rings [12,13]. However, g-C₃N₄ is considered the most stable allotrope under ambient conditions [14,15]. Furthermore, Kroke et al. [16] determined by DFT calculations that the structure of tri-s-triazine is 30 kJ mol⁻¹ more stable than s-triazine, mainly due to an electronic connection of nitrogen atoms. The g-C₃N₄ structure shows certain similarity with graphene because both of them are 2D materials with alternative sp²/sp³ hybridized conjugated carbon atoms, but the layers in g-C₃N₄ are linked by Van der Waals forces with a distance between them of 3.29 Å and thereby, it may be considered as a graphite-like structure ending in NH and NH₂ groups [17,18]. Moreover, the existence of nitrogen atoms into carbon skeleton can improve the physicochemical properties, since they can act as electron donor sites to enhance photocatalytic conductivity [18].

In general, the g-C₃N₄ synthesis is described as a combination of polyaddition and polycondensation reactions involving a N-rich precursor, which yields long extended 2D networks of triazine/heptazine repeating units. Among other synthetic parameters, the selection of the N-rich precursor influences on the morphology, electronic structure and surface chemistry, and consequently, the photoactivity of synthesized g-C₃N₄. The most reported precursors in literature were dicyandiamide, melamine, thiourea, urea, among others, which are abundant monomers that generate non-toxic polymeric g-C₃N₄ [12]. Nguyen et al. [19] reported a thermal synthesis method followed by chemical oxidation for the synthesis of water-dispersible photocatalysts from thiourea, showing a high activity for the methylene blue removal. In the same way, Oh et al. [20] demonstrated that polymerization of urea by sequential heating resulted in faster kinetics and enhanced photodegradation of Rhodamine B. Liang et al. [21] found that g-C₃N₄ synthesized from urea exhibited an enhanced catalytic activity for photoreduction of Cr(VI), while Dong et al. [22] pointed out that the type of precursor is one of the main factors to prepare high activity photocatalysts. Recently, Torres-Pinto et al. [23] studied different precursors for a microwave-assisted synthesis method, concluding that urea was the most recommended precursor to prepare g-C₃N₄ with improved photoactivity for the phenol degradation and H₂O₂ production.

In this work, g-C₃N₄ was synthesized by a one-pot thermal synthesis from the most used N-rich precursors in literature. The physicochemical and optical properties of g-C₃N₄ materials were analyzed with special attention to unveil the role of the precursor on the band gap energy and less and more g-C₃N₄ condensed structures, such as melem or melon ones. In addition, the photoactivity of the samples was assessed for the photodegradation of 5-FU and CP in aqueous solution and a mixture of both cytostatic drugs under different irradiation sources, in particular near UV-Vis and solar-LED.

2. Materials and methods

2.1. Synthesis of graphitic carbon nitride

Graphitic carbon nitride (g-C₃N₄) was synthesized by a one-pot thermal decomposition from different N-rich precursors such as cyanamide (CY), dicyandiamide (DCY), melamine (M), thiourea (TU) and urea (U), adapting a methodology described in a previous work [24]. Cyanamide, thiourea and urea were selected as starting molecules of the synthetic pathway, and dicyandiamide and melamine as reaction intermediates. The list of chemicals and details regarding the material synthesis can be found in Supporting Information (Section S1).

2.2. Characterization techniques

g-C₃N₄ materials were characterized by a set of complementary techniques (ATR-FTIR, Raman spectroscopy, XRD, STEM, XPS, DRUV, N₂ physisorption and point of zero charge – pH_{PZC} –) to determine physical (porosity, surface area, morphology, crystalline phase, etc), chemical (bulk and surface composition) and optical (band gap) properties, according to the procedures and methods detailed in the Supporting Information (Section S2) and elsewhere [25–30].

2.3. Photocatalytic reactions

The photocatalytic activity of the synthesized materials was assessed for the degradation of cyclophosphamide (CP) and 5-fluorouracil (5-FU) in aqueous solutions under both near UV-Vis and solar-LED irradiations. The experiments were performed in a glass reactor with 100 mL of solution containing 5-FU (10 mg L⁻¹ or 76.9 μ mol L⁻¹) or CP (10 mg L⁻¹ or 38.3 μ mol L⁻¹) pollutants, or a mixture of 5-FU and CP (5 mg L⁻¹/each) and a catalyst concentration of 1 g L⁻¹. The concentration of 5-FU and CP was monitored by ultra-high performance liquid chromatography (UHPLC). More details regarding the photocatalytic experiments and analysis method for the pollutants are described in Supporting Information (Section S3).

3. Results and discussion

3.1. Materials characterization

The transformation of the different N-rich precursors into g-C₃N₄ depended on the type of selected starting molecule. In Fig. 1 is shown the reaction pathway, in which CY, U and TU are starting molecules, while DCY is a reaction intermediate from CY and M is a common intermediate from all of them. For simplicity, the formation of less and more condensed g-C₃N₄ structures through the clustering of only heptazine units is depicted in Fig. 1, because this phase is considered the most stable under ambient conditions. It is well-known the formation of heptazine (or s-triazine) units occurs via rearrangements of melamine molecules, evolving different gases as CO₂, NH₃, CS₂ and H₂S at different temperatures [31], and after that, the polymeric g-C₃N₄ structure is obtained at ~520 °C through the further condensation of the heptazine units [12,32]. In the one-pot thermal synthesis, 550 °C was selected to complete the transformation of the selected N-rich precursor into g-C₃N₄, and taking into account that it is thermally unstable between 600 and 700 °C, beyond which the g-C₃N₄ structure disappears evolving nitrogen and cyano fragments.

At a first glance, the yield of g-C₃N₄ evidently depended on the chemical composition of each selected N-rich precursor (Table 1), M and DCY, as expected in a weight base (g/g), showing the highest yields (~59%) and TU and U the lowest values (~14% and 10%, respectively). This fact is in agreement with several works in literature indicating a low degree of polymerization or even, the presence of defects in the corresponding g-C₃N₄ prepared from both TU and U monomers [31,33]. On the other hand, and for a fair comparison, the abundance and the price of the different N-rich monomers should be considered, once the experimental conditions were maintained constant during the material synthesis. Thus, the order of preference should be DCY = M > U > TU > CY. Nevertheless, other aspects related with the structure and physicochemical properties of the obtained materials, as well the performance on the required application should be investigated.

The morphology of the samples was analyzed by STEM. Fig. 2 shows STEM images of g-C₃N₄ photocatalysts, main differences being attributed to the thermal decomposition pathway. Thus, two main structures can be clearly identified depending on the type of N-rich precursor used. In the case of oxygen-containing urea and sulfur-containing thiourea, a thin crumpled paper-like structure with small flat sheets and wrinkles is observed (Fig. 2a and c, respectively). These samples even show the

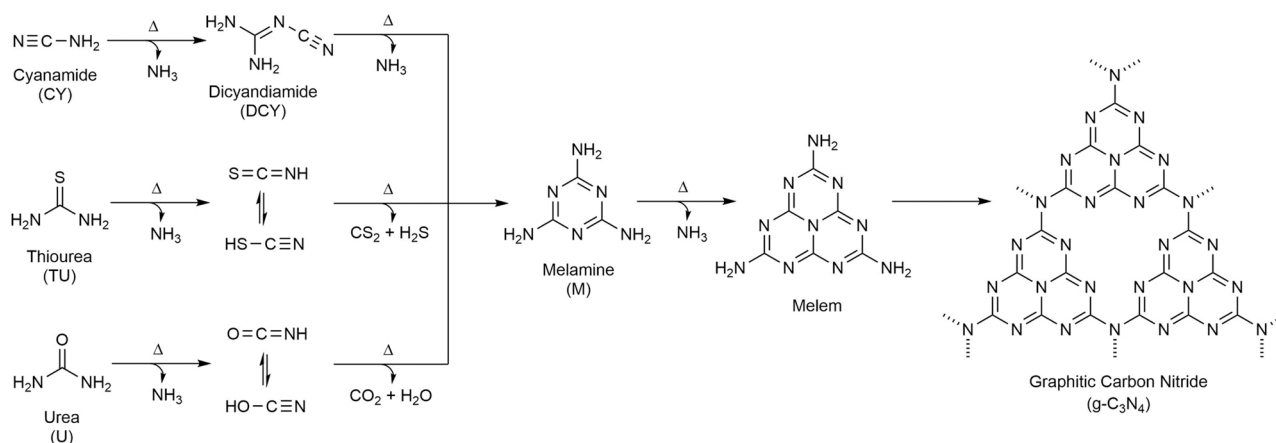


Fig. 1. Reaction pathway of g-C₃N₄ from cyanamide, urea, thiourea, dicyandiamide and melamine precursors. Adapted from Ong et al. [12].

Table 1

Yield and textural properties of the synthesized photocatalysts.

Samples	Yield (%)	S _{BET} (m ² g ⁻¹)	V _{meso} (cm ³ g ⁻¹)	V _{total} (cm ³ g ⁻¹)	L _{crystal} (nm)	d _{layer} (Å)	Number of layers
CY	20.6	13	0.029	0.176	3.9	3.295	12
DCY	58.7	7	0.024	0.096	4.9	3.274	15
M	59.0	< 5	0.022	0.061	6.3	3.266	19
TU	13.9	15	0.030	0.150	4.0	3.281	12
U	10.0	39	0.031	0.373	2.9	3.302	9

S_{BET} = BET surface area; V_{meso} = mesopore volume; V_{total} = total pore volume; L_{crystal} = crystallite size; d_{layer} = interlayer spacing.

presence of large voids or interstitial spaces, as consequence of the large amount of pyrolysis gases released (e.g. NH₃, CO₂, H₂S) during the synthesis procedure, which could act as templates [12]. On contrast, DCY and M displayed aggregates of flake sheets with a smooth and slack surface without appreciated voids (Fig. 2d and e, respectively). Finally, g-C₃N₄ prepared from cyanamide exhibited a combination of both structures, i.e., smaller and fluffier flat sheets with other large flakes (Fig. 2f). Of note, the formation and arrangement of these different structures will have a significant effect on the corresponding textural properties. On the other hand, a homogenous distribution of carbon and nitrogen atoms was observed throughout the g-C₃N₄ surface, as observed in the mapping of the U sample as an example (Fig. 2b).

The textural properties of the synthesized materials was evaluated by N₂ physisorption at -196 °C. Fig. 3 depicts the N₂ adsorption isotherms of g-C₃N₄ obtained from the different N-rich precursors. In general, all materials showed isotherms classified as type-II and type-IV in concordance with IUPAC classification, which designates the low porosity of the samples [17,34] and the formation of interstitial pores in the mesoporosity range [35], respectively. In fact, the N₂ volume adsorbed at very low relative pressure (P/P₀) was negligible as a result of the micropore absence in the samples. As previously observed by TEM, the presence of large mesopores was corroborated by the high N₂ volume adsorbed at high P/P₀ and a small hysteresis loop of type-H3, attributable to agglomerates composed by plate-like particles or materials with slit-shaped pores [24,30].

In general, all prepared g-C₃N₄ materials presented a very low porosity regardless the type of precursor employed. BET surface areas (S_{BET}) were between 4 and 39 m² g⁻¹, while the total pore volume (V_T) was in the range 0.061 and 0.373 cm³ g⁻¹ (Table 1) depending on the morphology and the size of the g-C₃N₄ sheets, as previously observed. Thus, large flake sheets displayed for M and DCY led to the lowest porosity (S_{BET} and V_T) [19,21]. On the contrary, the presence of

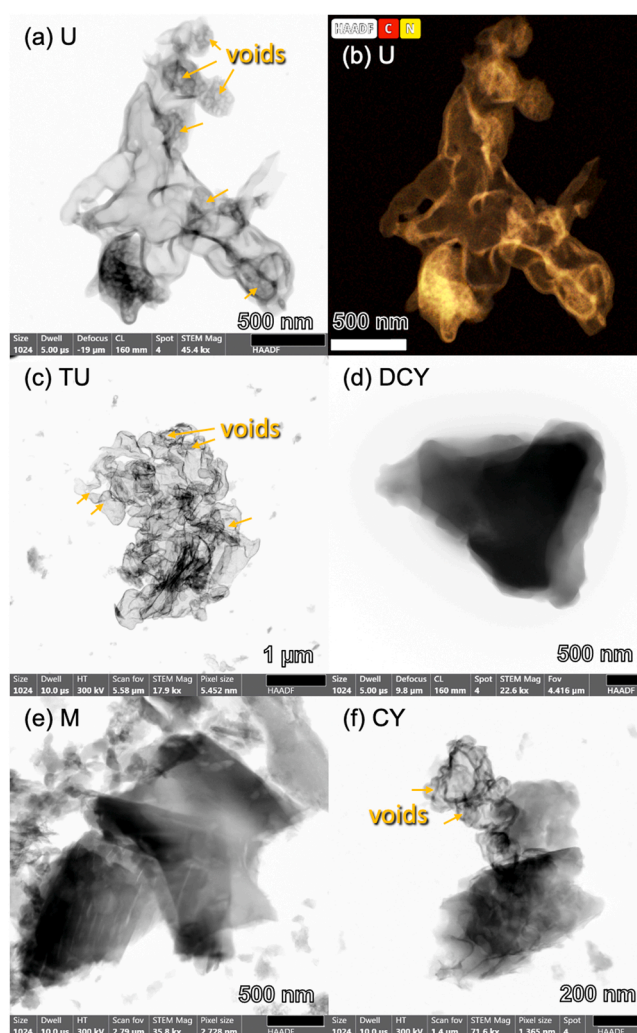


Fig. 2. STEM micrographs of (a) U, (c) TU, (d) DCY, (e) M and (f) CY. A STEM mapping is also included for U (b).

additional heteroatoms (regarding C and N), such as oxygen-containing and sulfur-containing monomers, promoted the formation of porous aggregates as consequence of the large amount of volatile products (i.e., CO₂, H₂O, NH₃, CS₂) generated during the thermal polycondensation of heptazine or s-triazine units, which could act as soft templates.

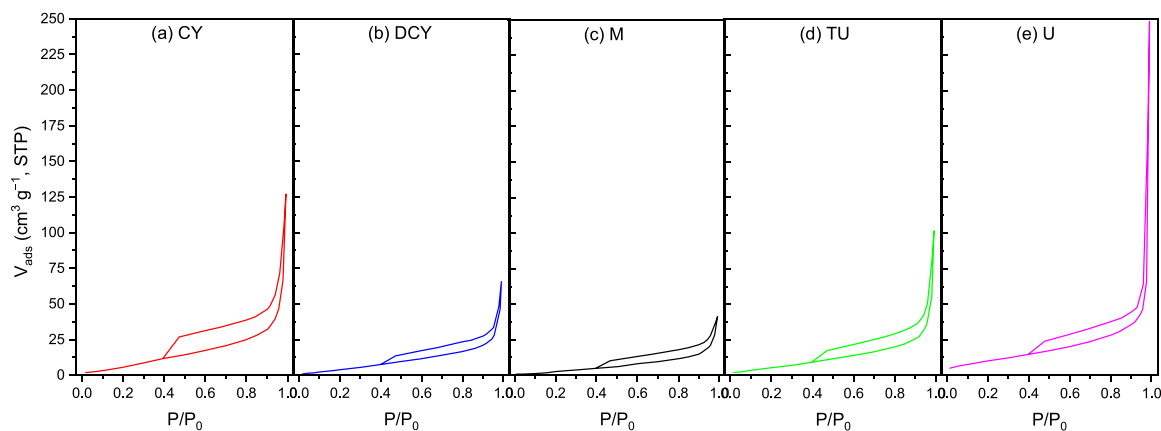


Fig. 3. N_2 adsorption-desorption isotherms of (a) CY, (b) DCY, (c) M, (d) TU and (e) U.

Therefore, structures of small flat sheets and wrinkles obtained with U and TU favoured the largest porosity, namely for U, whose S_{BET} increased almost ten-folds compared to M (i.e., 4 and $39 \text{ m}^2 \text{ g}^{-1}$ for M and U, respectively). Concerning the mesopore volume (V_{meso}), the same trends were identified depending on the type of structure and size formed during the synthesis. In general, the textural properties, namely S_{BET} , of the different $g\text{-C}_3\text{N}_4$ materials is comparable with the values reported in literature for other synthesis (Table S1).

XRD patterns of the different $g\text{-C}_3\text{N}_4$ samples are depicted in Fig. 4a. All materials presented two peaks at $2\theta \sim 12.6$ and $\sim 27.2^\circ$ corresponding to the (100) and (002) diffraction planes and due to in-plane heptazine structural packing and the interlayer stacking of $g\text{-C}_3\text{N}_4$, respectively (JCPDS 87-1526) [14,36]. On the other hand, the absence of any XRD peak placed at $\sim 17.5^\circ$ corresponding to the diffraction plane of the *s*-triazine units of the aromatic system [37,38], should confirm the major occurrence of the heptazine phase in the different $g\text{-C}_3\text{N}_4$ materials. In general, a higher intensity in the first peak is related to the formation of polymeric units, while a weak peak is associated to the presence of surface defects and less planar and amorphous character [23]. On the other hand, the sharp peak at $\sim 27.2^\circ$ is related with more regular repetitions between graphenic layers of graphitic structure, following the order melamine > dicyandiamide = thiourea > cyanamide > urea. The lowest crystallinity of U could be due to the presence of oxygen atoms, which evolved a large amount of gases (CO_2 , H_2O and NH_3) during the synthesis and inhibited the crystal growth [17]. The crystallite size (L_{crystal}) and interlayer spacing (d_{layer}) for the different $g\text{-C}_3\text{N}_4$ materials were also determined and collected in Table 1, the largest crystallites and lowest interlayer spacing being

obtained for M and DCY. In general, the crystallite size obtained for the different $g\text{-C}_3\text{N}_4$ materials was lower than that reported in literature for the same N-rich precursor (Table S1). Furthermore, the number of $g\text{-C}_3\text{N}_4$ layers estimated from the XRD parameters varied between 9 and 19 layers (Table 1), increasing as follows: $U < TU = CY < DCY < M$. Therefore, it seems that dicyandiamide and melamine favoured a higher number of more condensed $g\text{-C}_3\text{N}_4$ layers, while U promoted a few layers of less condensed structures.

ATR-FTIR spectra of all synthesized materials showed typical peaks or bands from the stretching vibration of $g\text{-C}_3\text{N}_4$ heterocycles and amine (N-H) groups (Fig. 4b). The peaks placed at 806 and 887 cm^{-1} are characteristic of $g\text{-C}_3\text{N}_4$ materials and associated to the vibrational modes of heptazine rings [21,39]. The bands at around 1240 , 1330 and 1417 cm^{-1} are assigned to stretching vibrations of C–N–C bridging bonds between amine groups and heptazine rings [40], whereas the peaks at 1562 and 1645 cm^{-1} are ascribed to C=N bonds [23]. The broad band between 3000 and 3500 cm^{-1} belongs to stretching modes of N–H or O–H bonds, due to the residual NH or NH_2 groups or adsorbed water molecules, respectively [19,41]. In general, all materials presented the characteristic bands of the $g\text{-C}_3\text{N}_4$ structure without appreciable differences among the different N-rich precursors.

Since all samples exhibited comparable ATR-FTIR results, the spectral properties were also investigated from Raman spectra, which showed some peaks between 400 and 1300 cm^{-1} ascribed with the vibration modes of $g\text{-C}_3\text{N}_4$ aromatic units (Fig. 5). As a rule for carbon-based materials, Raman peaks at $1550 - 1590$ and $1310 - 1350 \text{ cm}^{-1}$ correspond to the graphitic band occurring from the bond stretching of $\text{sp}^2\text{-C}$ atoms and the defect activated band, respectively [42,43]. The D

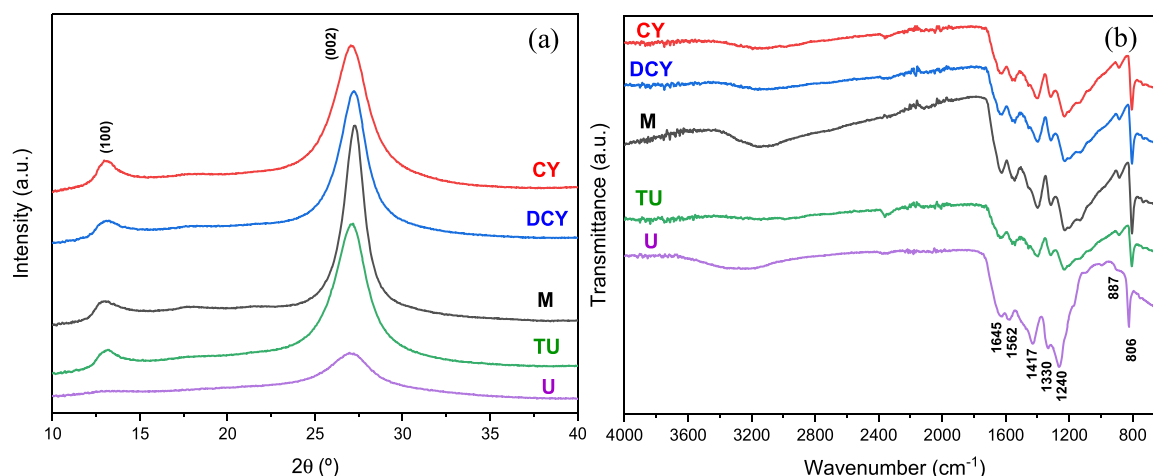


Fig. 4. (a) XRD patterns and (b) ATR-FTIR spectra of $g\text{-C}_3\text{N}_4$ photocatalysts.

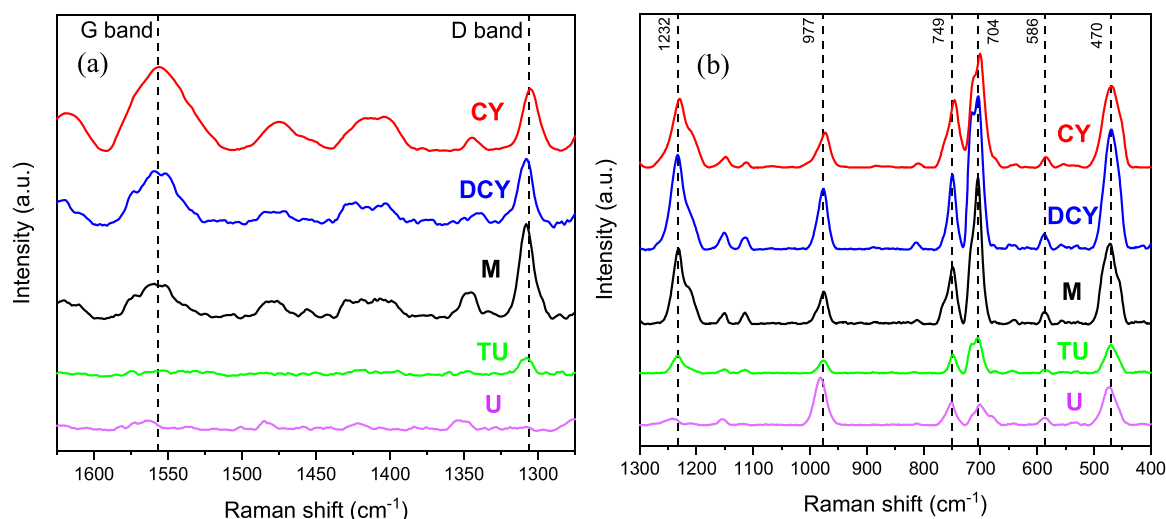


Fig. 5. Raman spectra recorded between (a) 1600 – 1300 cm^{-1} and (b) 1300 – 400 cm^{-1} of $\text{g-C}_3\text{N}_4$ materials obtained with 785 nm laser.

and G bands of $\text{g-C}_3\text{N}_4$ placed at ~ 1305 and ~ 1555 cm^{-1} are due to disordered sp^2 microdomains incorporated by the linking with nitrogen atoms and the vibrational mode in graphite-like structures, respectively [44]. In general, D and G bands showed a low intensity for all $\text{g-C}_3\text{N}_4$ materials (Fig. 5a), those for U and TU being really difficult to discriminate from the background noise and fluorescence interference. In fact, the absence of D and/or G bands was also reported by $\text{g-C}_3\text{N}_4$ materials [41,45,46]. The intensity ratio of D and G bands (I_D/I_G) was observed to increase as follows: $\text{CY} < \text{DCY} < \text{M}$ (Table 2), which means that the generation of more condensed $\text{g-C}_3\text{N}_4$ networks is favoured by high I_D/I_G ratios [47,48], i.e., with dicyandiamide and melamine precursors.

On the other hand, other peaks observed in Raman spectra give important information about $\text{g-C}_3\text{N}_4$ structure (Fig. 5b). The strong peaks placed at ~ 704 and ~ 749 cm^{-1} correspond to the bending vibrations of melon oligomers, while the bands at ~ 470 , ~ 586 and ~ 977 cm^{-1} are ascribed to heptazine ring vibration in melon/melon units. Analogously to the I_D/I_G ratio, the intensity ratios calculated at 749 and 704 cm^{-1} (I_{749}/I_{704}) and at 586 and 470 cm^{-1} (I_{586}/I_{470}) provide information about the layer-layer deformation vibrations [49]. High I_{749}/I_{704} or I_{586}/I_{470} ratios corresponded to $\text{g-C}_3\text{N}_4$ materials formed by individual or few layers and thereby, urea would be the optimal precursor to obtain individual $\text{g-C}_3\text{N}_4$ layers, while M and DCY with the lowest ratios should possess a large number of layers. These observations are in agreement with the number of layers determined from XRD. Finally, the sharp peak placed at 1232 cm^{-1} corresponds to typical stretching vibration of C–N and C=N heterocycles [41,46].

The surface chemical composition of $\text{g-C}_3\text{N}_4$ materials was studied in-depth by XPS. The high-resolution spectra corresponding to C1s and N1s regions are depicted in Fig. 6, while the surface chemical composition (C, N, O) is gathered in Table 2. The surface $\text{C}_{\text{XPS}}/\text{N}_{\text{XPS}}$ atomic ratio was also determined for the different samples and resulted to be higher than the stoichiometric C/N value of $\text{g-C}_3\text{N}_4$ (i.e., 0.75) [12]. This

fact was described to enhance the photoactivity due to the creation of abundant nitrogen vacancies, in comparison with nitrogen atoms linked to form heptazine units [50]. Among $\text{g-C}_3\text{N}_4$ materials, M and DCY presented the lowest $\text{C}_{\text{XPS}}/\text{N}_{\text{XPS}}$ ratio, which would be explained by a structure formed of more condensed heptazine units, in agreement with Raman results. In all cases, a residual oxygen content was detected and due to some oxygen-functionalities incorporated during the synthesis or water molecules adsorbed at the surface.

For the sake of analyzing whether the incorporation of surface chemical functionalities depends on the type of N-rich precursor, the C1s and N1s regions were deconvoluted in Fig. 6. In this context, the C1s spectra were deconvoluted in four components (Fig. 6a), the first component placed at ~ 284.8 eV corresponds to the typical adventitious carbon (Advent. C), such as carbon impurities or defects of sp^2 -C atoms in the samples [51,52], while the second one at ~ 286.2 eV corresponds to C–(N)₃ bonds from sp^3 -C atoms bonded nitrogen atoms in heptazine rings [23,52]. The third peak placed at ~ 288.2 eV was attributed to sp^2 -C atoms from N=C–N bonds, while the last peak was assigned to the presence of residual carbonates [19,43], as well as some C–O and/or C=O containing groups could have certain contribution to the previous assigned peaks. Concerning the N1s spectra (Fig. 6b), the deconvolution was carried out on three peaks at ~ 398.7 , ~ 400.0 and ~ 401.2 eV ascribed to C–N=C bonds from sp^2 -N in the heptazine rings, tertiary nitrogen atoms from N–(C)₃ bonds, and residual amino groups (C–N–H), respectively [20]. For the TU sample, a fourth peak at 402.5 eV corresponding to terminal nitro groups was also identified [23].

The incorporation of different chemical functionalities is evidenced in Fig. 7. The formation of partially condensed polymeric melon or melon oligomers containing terminal amine groups and more condensed heptazine units with tertiary N–(C)₃ bonds can be determined from the N1s deconvolution [20]. The N–(C)₃/C–N–H ratio for the different $\text{g-C}_3\text{N}_4$ materials decreased as follows: $\text{M} (2.00) > \text{DCY} (1.92) \geq \text{CY} (1.84) > \text{TU} (1.47) \geq \text{U} (1.46)$. J. Oh et al. [20] reported that $\text{g-C}_3\text{N}_4$

Table 2
Chemical and optical properties of the $\text{g-C}_3\text{N}_4$ samples.

Samples	I_D/I_G	I_{749}/I_{704}	I_{586}/I_{470}	C_{XPS} (%)	N_{XPS} (%)	O_{XPS} (%)	$\text{C}_{\text{XPS}}/\text{N}_{\text{XPS}}$ ratio	pH_{PZC}	E_g (eV)
CY	0.83	0.61	0.18	51.0	44.6	4.4	1.14	6.1	2.70
DCY	1.11	0.51	0.18	48.8	48.5	2.7	1.01	4.9	2.68
M	1.64	0.42	0.22	47.3	50.0	2.7	0.95	5.8	2.68
TU	-	0.55	0.18	52.1	42.9	5.0	1.21	5.0	2.73
U	-	1.07	0.25	55.3	40.4	4.3	1.37	5.2	2.90

I_D/I_G , I_{749}/I_{704} , I_{586}/I_{470} = intensity ratios at selected Raman shifts; C_{XPS} , O_{XPS} , N_{XPS} = atomic surface content determined by XPS; pH_{PZC} = point of zero charge; E_g = band gap energy.

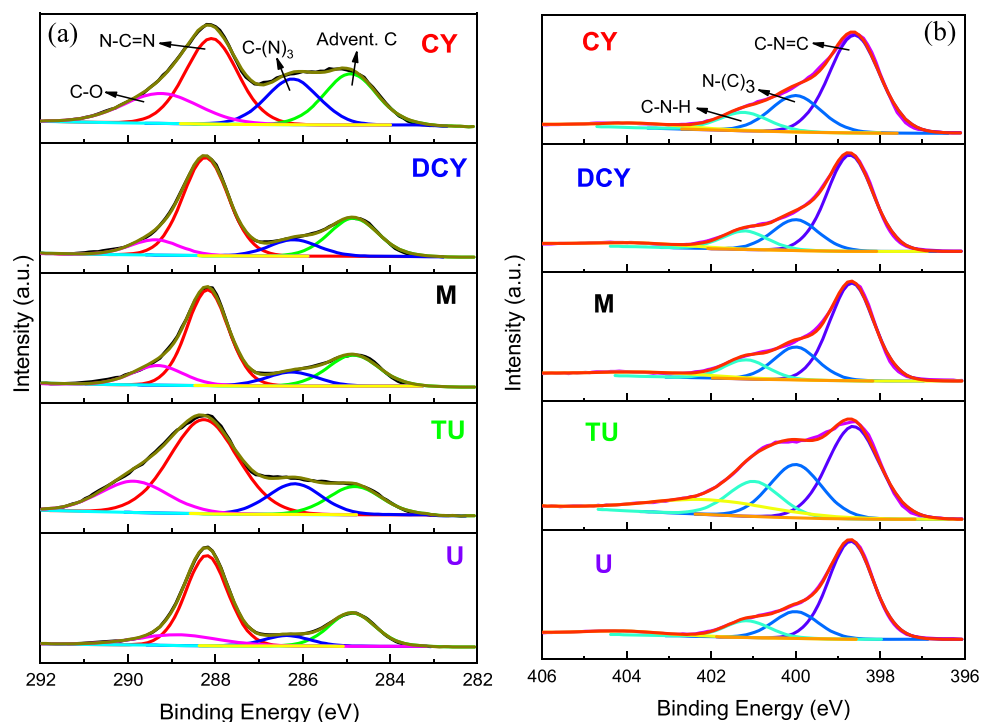


Fig. 6. High-resolution XPS spectra and deconvolution of (a) C1s and (b) N1s regions of prepared photocatalysts.

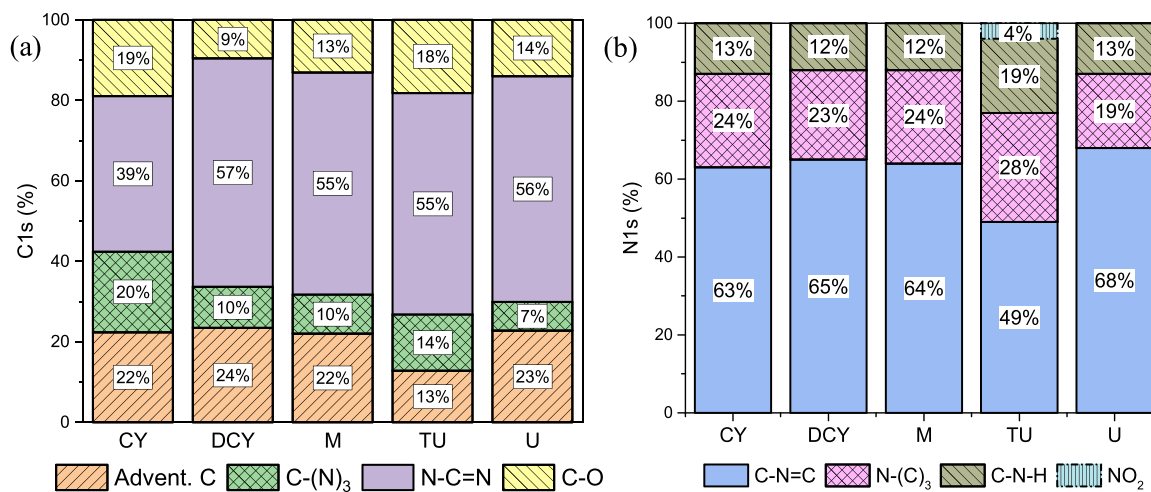


Fig. 7. Species percentages of the g-C₃N₄ materials determined from the deconvolution of (a) C1s and (b) N1s regions.

from DCY presented the highest N-(C)₃/C-N-H ratio and followed of M, whereas U possessed the lowest value. Therefore, M and DCY seem to favour the formation of more condensed g-C₃N₄ networks, while U and TU could provide more melem or melon structures. Finally, the pH_{PZC} of synthesized materials was determined and showed a slightly acidic character with values between 4.9 and 6.1. (Table 2).

The UV-Vis diffuse reflectance spectra of synthesized materials, expressed in terms of Kubelka-Munk (K-M) absorption units, are shown in Fig. 8a. All g-C₃N₄ photocatalysts showed a strong intensive absorption band in the visible range, associated with π-π* transitions of conjugated ring system [24]. The lowest UV-Vis absorption of U and TU could be related with the occurrence of less condensed melem or melon oligomers. On the other hand, Tauc's plots were used to calculate the band gap (E_g) of prepared materials (Fig. 8b). In general, the band gaps were narrow in the range of 2.68 and 2.90 eV (Table 2), being U with the highest E_g, which may be attributed to a low crystalline structure of less

condensed oligomer layers, in agreement with XRD, Raman and XPS analysis. In fact, the low crystallinity of g-C₃N₄ can motivate an increase of the π-π* stacking distance and, consequently, to a larger band gap and faster charge recombination [53]. On the other hand, a more connected structure of g-C₃N₄ resulted in a larger overlapping of the aromatic p-orbitals [54], which allowed to obtain a reduced E_g ~2.7 eV, which is in agreement with those values reported often in literature for the selected N-rich precursors (Table S1).

3.2. Photocatalytic degradation of 5-FU and CP under near UV-Vis and solar-LED irradiations

The photocatalytic activity of g-C₃N₄ photocatalysts for the 5-FU and CP degradation under near UV-Vis or solar-LED irradiations are depicted in Fig. 9b-d. The pollutants conversion (X,%), kinetic rate constant (k_{app}), and regression coefficient (r²) are gathered in Table 3. Firstly, the

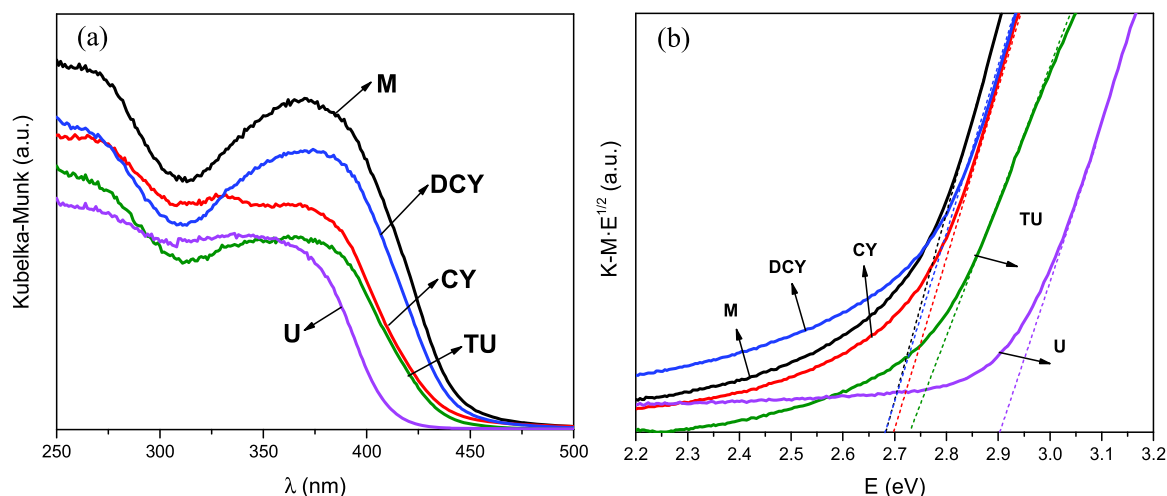


Fig. 8. (a) UV-Vis spectra and (b) Tauc's plots vs. energy (eV) of prepared photocatalysts.

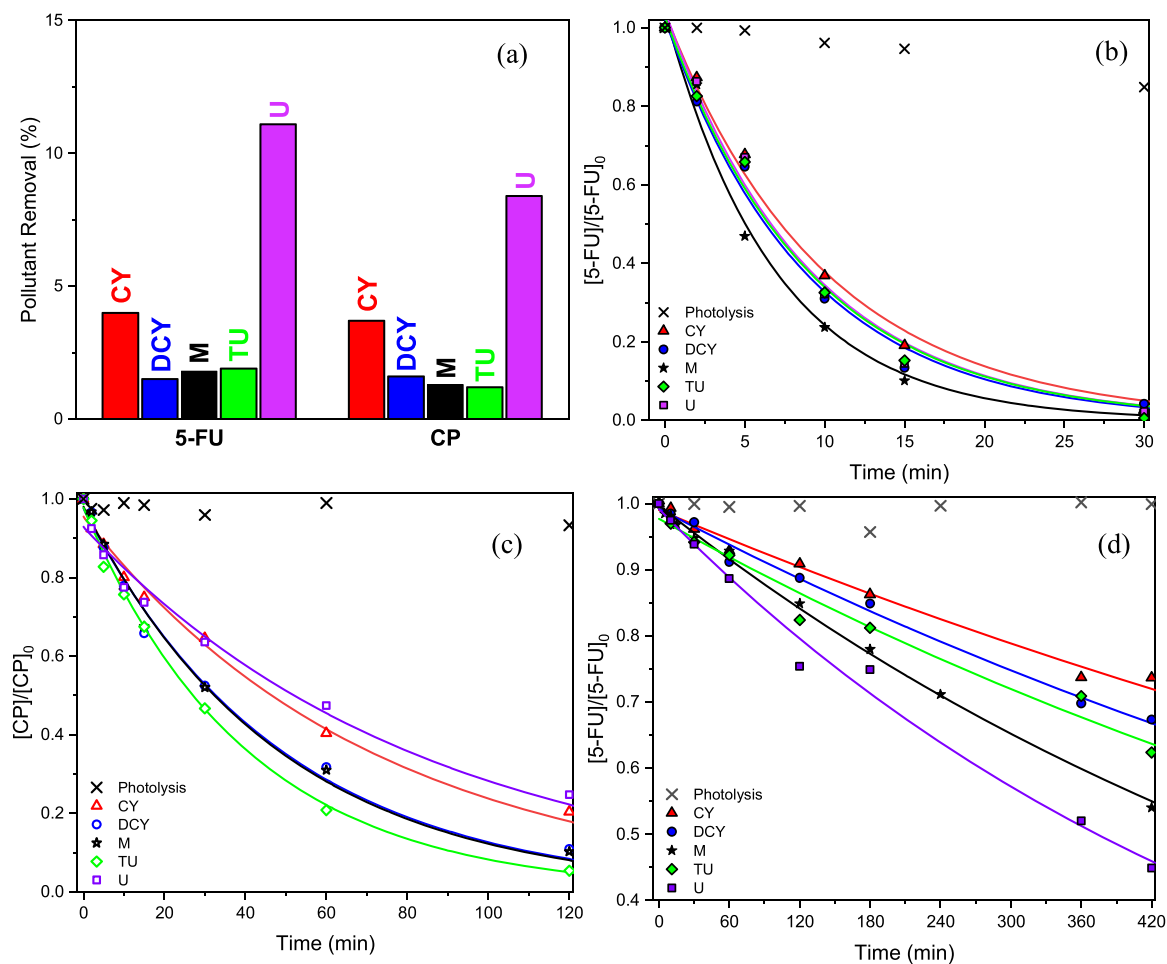


Fig. 9. Removal of 5-FU and CP as a function of time for the synthesized g-C₃N₄ by (a) adsorption at 30 min, (b, c) photocatalysis under near UV-Vis and (d) solar-LED irradiations.

adsorption-desorption equilibrium in dark conditions was established for all samples after 30 min at room temperature for both contaminants. The adsorption capacity of 5-FU was 4.0%, 1.5%, 1.8%, 1.9% and 11.1% for CY, DCY, M, TU and U (Fig. 9a), respectively, while the adsorption of CP was lower (i.e., 1.2 – 8.4%). In general, the textural properties (S_{BET} and V_{total} , Table 1) of the materials were well-correlated with the

adsorption capacity, since U was the most porous material with the highest pollutants removal. Once saturated the photocatalysts, the pollutant removal should be only due to the photocatalytic efficiency. In the absence of photocatalysts (i.e., photolysis), the degradation of both pollutants was negligible under near UV-Vis and solar-LED irradiations (Fig. 9b-c). Nevertheless, almost total degradation of 5-FU within

Table 3

Pollutant conversion ($X_{X \text{ min}}$), kinetic rate constant (k_{app}) and regression coefficient (r^2) of 5-FU and CP degradation under near UV-Vis and solar-LED irradianations at different conditions.

Catalyst	5-FU						CP		
	Near UV-Vis			Solar-LED			Near-UV/Vis		
	$X_{30 \text{ min}}$ (%)	$k_{app} \times 10^{-2}$ (min^{-1})	r^2	$X_{420 \text{ min}}$ (%)	$k_{app} \times 10^{-4}$ (min^{-1})	r^2	$X_{120 \text{ min}}$ (%)	$k_{app} \times 10^{-2}$ (min^{-1})	r^2
Photolysis	15.1	-	-	0.4	-	-	6.7	-	-
CY	97.4	10.1	0.993	26.3	7.6	0.985	79.6	1.4	0.991
DCY	95.8	11.4	0.992	32.7	9.4	0.991	89.1	2.1	0.990
M	98.7	14.6	0.991	46.0	14.1	0.997	89.8	2.1	0.993
TU	99.4	11.1	0.992	37.6	10.2	0.972	94.6	2.5	0.993
U	97.7	11.1	0.989	55.1	18.3	0.989	75.3	1.2	0.975

30 min under near UV-Vis irradiation was obtained with all g-C₃N₄ materials regardless the N-rich precursor used (Fig. 9b). Only small differences were found in the kinetic rate constants (k_{app}), M showing the highest value of $14.6 \cdot 10^{-2} \text{ min}^{-1}$ (Table 3).

In the case of the CP pollutant, all g-C₃N₄ materials were also active with differences in the efficiency depending on the N-rich precursor (Fig. 9c). Thus, g-C₃N₄ synthesized from thiourea, dicyandiamide and melamine showed a CP degradation close to 95% in 180 min and thereby, structures of more condensed heptazine units (M and DCY) or individual melem or melon oligomers (TU) are active enough to remove both 5-FU and CP. By comparing both pollutants, CP was more difficult to degrade than 5-FU probably to the electrophile hydroxyl radicals generated by the photocatalysts, which prefer to attack molecules with a high density of electrons (i.e., C=C bonds) compared to aliphatic compounds like CP. The activity of all g-C₃N₄ materials for the photodegradation of 5-FU was also studied under solar-LED irradiation (Fig. 9d). In this case, the photolysis of 5-FU was more negligible, i.e., < 0.5%. Once again, all materials were active under these conditions due to their reduced band gap, the k_{app} increasing as follows: U > M > TU > DCY > CY (Table 3). The photoactivity of the samples could be justified by the combination of various effects: (i) surface area, (ii) well-connected g-C₃N₄ structures and (iii) high surface C_{XPS}/N_{XPS} ratios.

Finally, g-C₃N₄ materials derived from melamine and thiourea were selected to evaluate their efficiency in the photodegradation of an aqueous solution containing both 5-FU and CP contaminants under near UV-Vis and solar-LED irradianations (Fig. 10). Both photocatalysts were selected taking into account that TU presented mainly a structure formed by less condensed melem and melon oligomers, while M is typical precursor used due to a structure of more condensed heptazine units. Once again, CP was degraded slower than 5-FU regardless the material and the irradiation source used. In addition, both pollutants were removed to longer reaction times compared to an aqueous solution

containing each contaminant under both irradiation sources. Thus, the total removal of 5-FU and CP in the same solution was achieved at ~60 and ~180 min, respectively, using the M photocatalyst and near UV-Vis irradiation (Fig. 10a), while only ~30 and ~120 min were need to achieve similar removal values when the pollutants were tested separately (Table 3). Analogously, the experiments under solar-LED required longer reaction times for the photodegradation of both pollutants in the same solution (Fig. 10b vs. Table 3) than a solution with only one contaminant. These facts could be explained by a competitive effect between CP and 5-FU molecules by the generated hydroxyl radicals. On the other hand, the TU photocatalyst demonstrated to be more efficient than M to treat aqueous solutions containing both pollutants specifically under solar-LED, since TU showed a higher k_{app} for both contaminants (e.g., $k_{app, 5-FU} = 11.3 \times 10^{-4}$ and $8.8 \times 10^{-4} \text{ min}^{-1}$ for TU and M, respectively), which demonstrate that g-C₃N₄ materials with less condensed structures can be as active as typical more condensed g-C₃N₄ materials.

For comparison purposes, Table 4 summarizes studies regarding different photocatalysts recently published for the removal of 5-FU or CP cytostatic drugs. Some experimental details are listed, such as concentration, pollutant, the light source used, catalyst load, and the pollutant conversion at a given time. Of note, an accurate comparison of the material photoactivity prepared in this work with those collected in Table 4 is really difficult because of operating parameters, such as irradiation source, catalyst loading and pollutant concentration, among others, were different. For instance, the total 5-FU degradation was achieved in 180 min under UV-LED over g-C₃N₄/ZnO composites with a band gap around 3.00 – 3.15 eV and BET surface area ca. 10 – 30 m² g⁻¹ [24]. Swedha et al. [55] reported g-C₃N₄ embedded Ni₃(VO₄)₂/ZnCr₂O₄ by co-precipitation method showing a high BET surface area of 150 m² g⁻¹ and a reduced band gap of 2.3 eV, the total 5-FU degradation being obtained in 200 min under a full spectrum halogen lamp. By comparing,

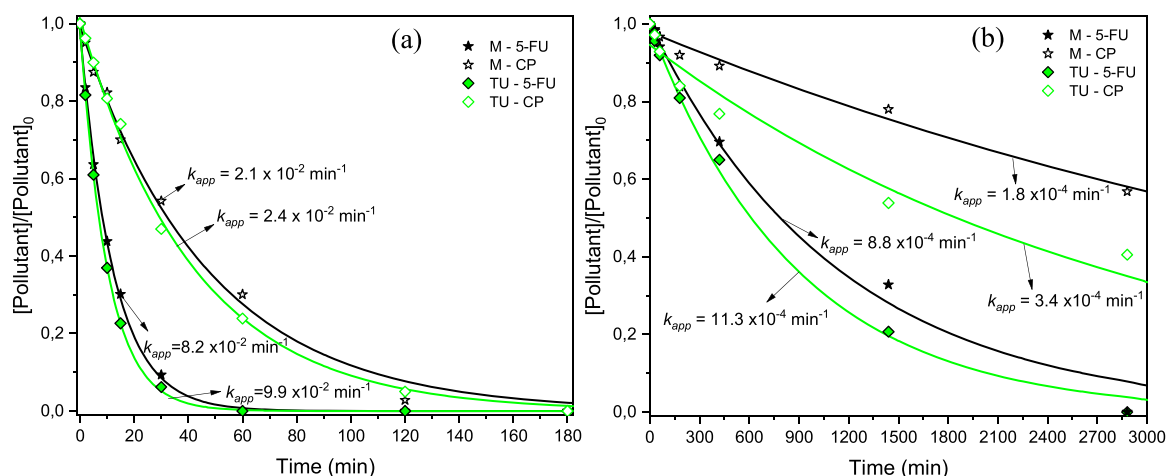


Fig. 10. Photocatalytic degradation of an aqueous solution containing both 5-FU and CP pollutants under (a) near UV-Vis and (b) solar-LED irradianations.

Table 4
Recently published works regarding photocatalysts for cytostatic drugs removal.

Photocatalyst	Irradiation source	Catalyst loading	Pollutant	Conversion (%) / time (min)	Ref.
P25	UV lamp ($\lambda > 254$ nm)	0.005 g L ⁻¹ 0.3 g L ⁻¹	5-FU - 200 μ g L ⁻¹ CP - 27.6 mg L ⁻¹	100 / 120 100 / 240	[4]
Bi-B doped TiO ₂	Xe-arc lamp ($\lambda > 420$ nm)	0.25 mg L ⁻¹	5-FU - 50 mg L ⁻¹ CP - 50 mg L ⁻¹	~95 / 240 ~70 / 240	[56]
Pt-TiO ₂	Xe-arc lamp ($\lambda > 290$ nm)	0.005 g L ⁻¹	CP - 50 mg L ⁻¹	100 / 60	[57]
N/S doped TiO ₂	Xe lamp ($\lambda > 300$ nm) solar-LED ($\lambda > 400$ nm)	0.1 g L ⁻¹	5-FU - 10 mg L ⁻¹	~80 / 180 ~40 / 360	[58]
TiO ₂ -TBMA	Xe lamp ($\lambda > 420$ nm) Medium pressure Hg lamp ($\lambda_{\text{max}} = 366$ nm)	0.5 g L ⁻¹	5-FU - 15 mg L ⁻¹	100 / 180 100 / 60	[59]
BiOCl	Medium pressure Hg lamp ($\lambda > 200$ nm)	0.2 g L ⁻¹	5-FU - 15 mg L ⁻¹	100 / 60	[60]
BiOClBr	Medium pressure Hg lamp ($\lambda > 200$ nm)	0.5 g L ⁻¹	5-FU - 15 mg L ⁻¹ CP - 15 mg L ⁻¹	100 / 90 79 / 120	[61]
g-C ₃ N ₄ /ZnO	UV-LED ($\lambda_{\text{max}} = 385$ nm)	1 g L ⁻¹	5-FU - 20 mg L ⁻¹	100 / 180	[24]
g-CNQDs/CuFe ₂ O ₄ /Cu ⁰	Xe lamp ($\lambda > 420$ nm)	0.2 g L ⁻¹	5-FU - 3.9 mg L ⁻¹	100 / 60	[62]
g-CN/Ni ₃ (VO ₄) ₂ /ZnCr ₂ O ₄	Halogen lamp ($\lambda > 200$ nm)	0.02 g L ⁻¹	5-FU - 20 mg L ⁻¹	100 / 200	[55]
g-C ₃ N ₄ (TU)	Medium pressure Hg lamp ($\lambda > 350$ nm)	1 g L ⁻¹	5-FU - 10 mg L ⁻¹ CP - 10 mg L ⁻¹	99 / 30 95 / 120	This work
g-C ₃ N ₄ (U)	solar-LED ($\lambda > 410$ nm)	1 g L ⁻¹	5-FU - 10 mg L ⁻¹	55 / 420	This work

TBMA= tributylmethylammonium; g-CN= graphitic carbon nitride; QDs= quantum dots

the photocatalysts of this work showed a good photoactivity for the degradation of 5-FU or CP under near UV-Vis and solar-LED irradiations compared to the described materials and those reported in literature (Table 4).

4. Conclusions

Graphitic carbon nitride (g-C₃N₄) was prepared by a one-pot thermal synthesis from different N-rich precursors. Melamine and dicyandiamide provided a low porous structure composed by large flake sheets with a smooth surface, whereas urea or thiourea favoured small flat sheets and wrinkles with a larger porosity, as consequence of volatile gases generated during thermal polycondensation. The major evidences of the role of N-rich precursor were obtained from XRD, Raman and XPS results. Thus, M and DCY displayed the highest I_D/I_G ratios leading to the generation of a high number of g-C₃N₄ layers composed of more condensed structures, while U and TU were better precursors to obtain individual melem or melon layers. In general, all materials presented narrow band gaps with a high light absorption in the visible range favoured by the overlapping of aromatic p-orbitals of g-C₃N₄ structures.

All g-C₃N₄ materials showed a high photoactivity for the degradation of 5-FU and CP under near UV-Vis and solar-LED irradiations. The total degradation of 5-FU was achieved for 30 min, while almost complete removal of CP was obtained for 120 min, which corroborated a more resistance to be degraded than 5-FU. The most active photocatalysts for both pollutants under near UV-Vis irradiation were M, DCY and TU, whereas U was the most active material for the 5-FU removal under solar-LED with half of the conversion for 420 min. Finally, TU and M were tested for the degradation of a solution containing both pollutants near UV-Vis and solar-LED irradiations, a competitive effect between pollutant molecules for the generated hydroxyl radicals being observed. Overall, the photoactivity of g-C₃N₄ materials can be justified by the combination of various effects: (i) surface area, (ii) well-connected and condensed g-C₃N₄ structures and (iii) high surface C_{XPS}/N_{XPS} ratios with nitrogen vacancies.

CRediT authorship contribution statement

Á. Pérez-Molina: Investigation, Conceptualization, Formal analysis, Methodology, Writing – original draft. S. Morales-Torres: Conceptualization, Data curation, Resources, Writing – review & editing, Supervision. L.M. Pastrana-Martínez: Conceptualization, Data curation, Resources, Writing – review & editing, Supervision. F.J. Maldonado-Hódar: Conceptualization, Resources, Project administration, Funding acquisition, Writing – review & editing, Supervision.

Declaration of Competing Interest

The authors declare that they have no known competing financial interests or personal relationships that could have appeared to influence the work reported in this paper.

Data Availability

Data will be made available on request.

Acknowledgements

This work was financially supported by the Spanish Projects, ref. RTI2018-099224-B-I00 from MCIN/AEI/10.13039/501100011033/FEDER “Una manera de hacer Europa”, FEDER/Junta de Andalucía-Consejería de Transformación Económica, Industria, Conocimiento y Universidades/B-RNM-486-UGR20 and Junta de Andalucía-Consejería de Universidad, Investigación e Innovación - Proyecto P21_00208. Á.P.-M. is grateful to MICIN/AEI/10.13039/501100011033 and the European Social Found (FSE) “El FSE invierte en tu futuro” for a predoctoral research contract (PRE2019-087946). S.M.-T. (RYC-2019-026634-I) and L.M.P.-M. (RYC-2016-19347) acknowledge the MICIN/AEI/10.13039/501100011033 and FSE “El FSE invierte en tu futuro” for their Ramón y Cajal research contracts. “Unidad de Excelencia Química Aplicada a Biomedicina y Medioambiente” of the University of Granada (UEQ—UGR) is gratefully acknowledged for the technical assistance. Funding for open access charge: Universidad de Granada / CBUA.

Appendix A. Supporting information

Supplementary data associated with this article can be found in the online version at [doi:10.1016/j.cattod.2023.114068](https://doi.org/10.1016/j.cattod.2023.114068).

References

- [1] A.L. Garcia-Costa, A. Alves, L.M. Madeira, M.S.F. Santos, Oxidation processes for cytostatic drugs elimination in aqueous phase: a critical review, *J. Environ. Chem. Eng.* 9 (2021), 104709.
- [2] T. Kosjek, S. Perko, D. Zigon, E. Heath, Fluorouracil in the environment: analysis, occurrence, degradation and transformation, *J. Chromatogr., A* 1290 (2013) 62–72.
- [3] S. Mukherjee, D. Mehta, K. Dhangar, M. Kumar, Environmental fate, distribution and state-of-the-art removal of antineoplastic drugs: a comprehensive insight, *Chem. Eng. J.* 407 (2021).
- [4] H.H.-H. Lin, A.Y.-C. Lin, Photocatalytic oxidation of 5-fluorouracil and cyclophosphamide via UV/TiO₂ in an aqueous environment, *Water Res.* 48 (2014) 559–568.

- [5] J. Zhang, V.W. Chang, A. Giannis, J.Y. Wang, Removal of cytostatic drugs from aquatic environment: a review, *Sci. Total Environ.* 445–446 (2013) 281–298.
- [6] C. Comminellis, A. Kapalka, S. Malato, S.A. Parsons, I. Poulous, D. Mantzavinos, Advanced oxidation processes for water treatment: advances and trends for R&D, *J. Chem. Technol. Biotechnol.* 83 (2008) 769–776.
- [7] S. Malato, P. Fernández-Ibáñez, M.I. Maldonado, J. Blanco, W. Gernjak, Decontamination and disinfection of water by solar photocatalysis: recent overview and trends, *Catal. Today* 147 (2009) 1–59.
- [8] M.N. Chong, B. Jin, C.W. Chow, C. Saint, Recent developments in photocatalytic water treatment technology: a review, *Water Res.* 44 (2010) 2997–3027.
- [9] D.S. Su, J. Zhang, B. Frank, A. Thomas, X. Wang, J. Paraknowitsch, R. Schlogl, Metal-free heterogeneous catalysis for sustainable chemistry, *ChemSusChem* 3 (2010) 169–180.
- [10] R.D. Huang, J. Wu, M.L. Zhang, B.Q. Liu, Z.Q. Zheng, D.X. Luo, Strategies to enhance photocatalytic activity of graphite carbon nitride-based photocatalysts, *Mater. Des.* 210 (2021) 110040–110061.
- [11] V. Devthade, D. Kulhari, S.S. Umare, Role of precursors on photocatalytic behavior of graphitic carbon nitride, *Mater. Today.: Proc.* 5 (2018) 9203–9210.
- [12] W.J. Ong, L.L. Tan, Y.H. Ng, S.T. Yong, S.P. Chai, Graphitic carbon nitride (g-C₃N₄)-based photocatalysts for artificial photosynthesis and environmental remediation: are we a step closer to achieving sustainability? *Chem. Rev.* 116 (2016) 7159–7329.
- [13] Y. Xu, S.P. Gao, Band gap of C₃N₄ in the GW approximation, *Int. J. Hydrog. Energy* 37 (2012) 11072–11080.
- [14] A. Thomas, A. Fischer, F. Goettmann, M. Antonietti, J.O. Muller, R. Schlogl, J. M. Carlsson, Graphitic carbon nitride materials: variation of structure and morphology and their use as metal-free catalysts, *J. Mater. Chem.* 18 (2008) 4893–4908.
- [15] Y. Wang, X. Wang, M. Antonietti, Polymeric graphitic carbon nitride as a heterogeneous organocatalyst: from photochemistry to multipurpose catalysis to sustainable chemistry, *Angew. Chem.* 51 (2012) 68–89.
- [16] E. Kroke, M. Schwarz, E. Horath-Bordon, P. Kroll, B. Noll, A.D. Norman, Tri-s-triazine derivatives. Part I. From trichloro-tri-s-triazine to graphitic C₃N₄ structures, *N. J. Chem.* 26 (2002) 508–512.
- [17] S. Paneri, P. Ganguly, B.N. Nair, A.A. Mohamed, K.G. Warriar, U.N. Hareesh, Role of precursors on the photophysical properties of carbon nitride and its application for antibiotic degradation, *Environ. Sci. Pollut. Res.* 24 (2017) 8609–8618.
- [18] D. Adekoya, S. Qian, X. Gu, W. Wen, D. Li, J. Ma, S. Zhang, DFT-guided design and fabrication of carbon-nitride-based materials for energy storage devices: a review, *Nano-Micro Lett.* 13 (2020).
- [19] T.K.A. Nguyen, T.T. Pham, N.P. Huy, E.W. Shin, The effect of graphitic carbon nitride precursors on the photocatalytic dye degradation of water-dispersible graphitic carbon nitride photocatalysts, *Appl. Surf. Sci.* 537 (2021) 148027–148038.
- [20] J. Oh, Y. Shim, S. Lee, S. Park, D. Jang, Y. Shin, S. Ohn, J. Kim, S. Park, Structural insights into photocatalytic performance of carbon nitrides for degradation of organic pollutants, *J. Solid State Chem.* 258 (2018) 559–565.
- [21] J. Liang, C. Jing, J. Wang, Y. Men, Photocatalytic reduction of Cr (VI) over g-C₃N₄ photocatalysts synthesized by different precursors, *Molecules* 26 (2021).
- [22] H. Dong, X. Guo, C. Yang, Z. Ouyang, Synthesis of g-C₃N₄ by different precursors under burning explosion effect and its photocatalytic degradation for tylosin, *Appl. Catal. B-Environ.* 230 (2018) 65–76.
- [23] A. Torres-Pinto, C.G. Silva, J.L. Faria, A.M.T. Silva, The effect of precursor selection on the microwave-assisted synthesis of graphitic carbon nitride, *Catal. Today* (2022).
- [24] Á. Pérez-Molina, L.M. Pastrana-Martínez, L.T. Pérez-Poyatos, S. Morales-Torres, F. J. Maldonado-Hódar, One-pot thermal synthesis of g-C₃N₄/ZnO composites for the degradation of 5-fluorouracil cytostatic drug under UV-LED Irradiation, *Nanomaterials* 12 (2022).
- [25] S. Brunauer, P.H. Emmett, E. Teller, Adsorption of gases in multimolecular layers, *J. Am. Chem. Soc.* 60 (1938) 309–319.
- [26] K.S.W. Sing, D.H. Everett, R.A.W. Haul, L. Moscou, R.A. Pierotti, J. Rouquerol, T. Siemieniowska, Reporting physisorption data for gas/solid systems with special reference to the determination of surface area and porosity, *IUPAC* 57 (1985) 603–619.
- [27] E.P. Barrett, L.G. Joyner, P.P. Halenda, The determination of pore volume and area distributions in porous substances. I. Computations from nitrogen isotherms, *J. Am. Chem. Soc.* 73 (1951) 373–380.
- [28] G. Newcombe, R. Hayes, M. Drikas, Granular activated carbon: Importance of surface properties in the adsorption of naturally occurring organics, *Colloids Surf. A* 78 (1993) 65–71.
- [29] L.M. Pastrana-Martínez, S. Morales-Torres, S.A.C. Carabineiro, J.G. Buijnsters, J. L. Figueiredo, A.M.T. Silva, J.L. Faria, Photocatalytic activity of functionalized nanodiamond-TiO₂ composites towards water pollutants degradation under UV/Vis irradiation, *Appl. Surf. Sci.* 458 (2018) 839–848.
- [30] S. Morales-Torres, L.M. Pastrana-Martínez, J.L. Figueiredo, J.L. Faria, A.M.T. Silva, Graphene oxide-P25 photocatalysts for degradation of diphenhydramine pharmaceutical and methyl orange dye, *Appl. Surf. Sci.* 275 (2013) 361–368.
- [31] G.G. Zhang, J.S. Zhang, M.W. Zhang, X.C. Wang, Polycondensation of thiourea into carbon nitride semiconductors as visible light photocatalysts, *J. Mater. Chem.* 22 (2012) 8083–8091.
- [32] X. Wang, K. Maeda, A. Thomas, K. Takanebe, G. Xin, J.M. Carlsson, K. Domen, M. Antonietti, A metal-free polymeric photocatalyst for hydrogen production from water under visible light, *Nat. Mater.* 8 (2009) 76–80.
- [33] Y. Zhang, J. Liu, G. Wu, W. Chen, Porous graphitic carbon nitride synthesized via direct polymerization of urea for efficient sunlight-driven photocatalytic hydrogen production, *Nanoscale* 4 (2012) 5300–5303.
- [34] Y.-P. Zhu, M. Li, Y.-L. Liu, T.-Z. Ren, Z.-Y. Yuan, Carbon-Doped ZnO Hybridized Homogeneously with Graphitic Carbon Nitride Nanocomposites for Photocatalysis, *J. Phys. Chem. C* 118 (2014) 10963–10971.
- [35] R.C. Bansal, J.B. Donnet, F. Stoeckli, *Active Carbon*, Marcel Dekker, New York, 1988.
- [36] F. Dong, Z. Zhao, T. Xiong, Z. Ni, W. Zhang, Y. Sun, W.K. Ho, In situ construction of g-C₃N₄/g-C₃N₄ metal-free heterojunction for enhanced visible-light photocatalysis, *ACS Appl. Mater. Interfaces* 5 (2013) 11392–11401.
- [37] P. Jiménez-Calvo, C. Marchal, T. Cottineau, V. Caps, V. Keller, Influence of the gas atmosphere during the synthesis of g-C₃N₄ for enhanced photocatalytic H₂ production from water on Au/g-C₃N₄ composites, *J. Mater. Chem. A* 7 (2019) 14849–14863.
- [38] J. Gao, Y. Zhou, Z. Li, S. Yan, N. Wang, Z. Zou, High-yield synthesis of millimeter-long, semiconducting carbon nitride nanotubes with intense photoluminescence emission and reproducible photoconductivity, *Nanoscale* 4 (2012) 3687–3692.
- [39] M. Kim, S. Hwang, J.S. Yu, Novel ordered nanoporous graphitic C₃N₄ as a support for Pt-Ru anode catalyst in direct methanol fuel cell, *J. Mater. Chem.* 17 (2007) 1656–1659.
- [40] P. Gibot, F. Schnell, D. Spitzer, Enhancement of the graphitic carbon nitride surface properties from calcium salts as templates, *Microporous Mesoporous Mater.* 219 (2016) 42–47.
- [41] T. Giannakopoulou, I. Papailias, N. Todorova, N. Boukos, Y. Liu, J. Yu, C. Trapalis, Tailoring the energy band gap and edges’ potentials of g-C₃N₄/TiO₂ composite photocatalysts for NO_x removal, *Chem. Eng. J.* 310 (2017) 571–580.
- [42] L.M. Pastrana-Martínez, S. Morales-Torres, V. Likodimos, J.L. Figueiredo, J. L. Faria, P. Falaras, A.M.T. Silva, Advanced nanostructured photocatalysts based on reduced graphene oxide-TiO₂ composites for degradation of diphenhydramine pharmaceutical and methyl orange dye, *Appl. Catal. B-Environ.* 123–124 (2012) 241–256.
- [43] L.M. Pastrana-Martínez, S. Morales-Torres, V. Likodimos, P. Falaras, J. L. Figueiredo, J.L. Faria, A.M.T. Silva, Role of oxygen functionalities on the synthesis of photocatalytically active graphene-TiO₂ composites, *Appl. Catal. B-Environ.* 158–159 (2014) 329–340.
- [44] X. Bai, L. Wang, Y. Wang, W. Yao, Y. Zhu, Enhanced oxidation ability of g-C₃N₄ photocatalyst via C₆₀ modification, *Appl. Catal. B-Environ.* 152–153 (2014) 262–270.
- [45] P. Niu, L.-C. Yin, Y.-Q. Yang, G. Liu, H.-M. Cheng, Increasing the visible light absorption of graphitic carbon nitride (Melon) photocatalysts by homogeneous self-modification with nitrogen vacancies, *Adv. Mater.* 26 (2014) 8046–8052.
- [46] Y. Yuan, L. Zhang, J. Xing, M.I. Utama, X. Lu, K. Du, Y. Li, X. Hu, S. Wang, A. Genc, R. Dunin-Borkowski, J. Arbiol, Q. Xiong, High-yield synthesis and optical properties of g-C₃N₄, *Nanoscale* 7 (2015) 12343–12350.
- [47] I. Ciria-Ramos, N. Navascués, F. Diaw, C. Furgeaud, R. Arenal, A. Ansón-Casaos, M. Haro, E.J. Juárez-Perez, Formamidineum halide salts as precursors of carbon nitrides, *Carbon* 196 (2022) 1035–1046.
- [48] S.E. Rodil, A.C. Ferrari, J. Robertson, W.I. Milne, Raman and infrared modes of hydrogenated amorphous carbon nitride, *J. Appl. Phys.* 89 (2001) 5425–5430.
- [49] J. Jiang, L. Ou-yang, L. Zhu, A. Zheng, J. Zou, X. Yi, H. Tang, Dependence of electronic structure of g-C₃N₄ on the layer number of its nanosheets: A study by Raman spectroscopy coupled with first-principles calculations, *Carbon* 80 (2014) 213–221.
- [50] H. Lan, L. Li, X. An, F. Liu, C. Chen, H. Liu, J. Qu, Microstructure of carbon nitride affecting synergetic photocatalytic activity: Hydrogen bonds vs. structural defects, *Appl. Catal. B-Environ.* 204 (2017) 49–57.
- [51] M.J. Lima, A.M.T. Silva, C.G. Silva, J.L. Faria, Graphitic carbon nitride modified by thermal, chemical and mechanical processes as metal-free photocatalyst for the selective synthesis of benzaldehyde from benzyl alcohol, *J. Catal.* 353 (2017) 44–53.
- [52] F. Dong, Y. Li, Z. Wang, W.-K. Ho, Enhanced visible light photocatalytic activity and oxidation ability of porous graphene-like g-C₃N₄ nanosheets via thermal exfoliation, *Appl. Surf. Sci.* 358 (2015) 393–403.
- [53] C. Li, J. Li, Y.B. Huang, J. Liu, M.M. Ma, K. Liu, C. Zhao, Z.J. Wang, S.C. Qu, L. Zhang, H.Y. Han, W.S. Deng, Z.G. Wang, Recent development in electronic structure tuning of graphitic carbon nitride for highly efficient photocatalysis, *J. Semicond.* 43 (2022) 021701–021715.
- [54] Y. Cui, J. Zhang, G. Zhang, J. Huang, P. Liu, M. Antonietti, X. Wang, Synthesis of bulk and nanoporous carbon nitride polymers from ammonium thiocyanate for photocatalytic hydrogen evolution, *J. Mater. Chem.* 21 (2011) 13032–13039.
- [55] M. Swedha, A.A. Alatar, M.K. Okla, I.A. Alaraidh, A. Mohebalidin, M. Aufy, L. L. Raju, A.M. Thomas, M.A. Abdel-Maksoud, S. Sudheer Khan, Graphitic carbon nitride embedded Ni₃(VO₄)₂/ZnCr₂O₄ Z-scheme photocatalyst for efficient degradation of p-chlorophenol and 5-fluorouracil, and genotoxic evaluation in *Allium cepa*, *J. Ind. Eng. Chem.* 112 (2022) 244–257.
- [56] A. Fiszka Borzyszkowska, A. Pieczyńska, A. Ofiarska, K. Nikiforow, P. Stepnowski, E.M. Siedlecka, Bi-B-TiO₂-based photocatalytic decomposition of cytostatic drugs under simulated sunlight treatments, *Sep. Purif. Technol.* 169 (2016) 113–120.
- [57] A. Ofiarska, A. Pieczyńska, A. Fiszka Borzyszkowska, P. Stepnowski, E. M. Siedlecka, Pt-TiO₂-assisted photocatalytic degradation of the cytostatic drugs ifosfamide and cyclophosphamide under artificial sunlight, *Chem. Eng. J.* 285 (2016) 417–427.
- [58] A. Koltsakidou, M. Antonopoulou, E. Epsilonigenidou, I. Konstantinou, A. E. Giannakas, M. Papadaki, D. Bikiaris, D.A. Lambropoulou, Photocatalytical

- removal of fluorouracil using TiO₂-P25 and N/S doped TiO₂ catalysts: a kinetic and mechanistic study, *Sci. Total Environ.* 578 (2017) 257–267.
- [59] P. Wilczewska, A. Pancielejko, J. Łuczak, M. Kroczeńska, W. Lisowski, E. M. Siedlecka, The influence of ILs on TiO₂ microspheres activity towards 5-FU removal under artificial sunlight irradiation, *Appl. Surf. Sci.* 573 (2022), 151431.
- [60] P. Wilczewska, A. Bielicka-Giełdoń, K. Szczodrowski, A. Malankowska, J. Ryl, K. Tabaka, E.M. Siedlecka, Morphology regulation mechanism and enhancement of photocatalytic performance of BiOX (X = Cl, Br, I) via mannitol-assisted synthesis, *Catalysts* 11 (2021) 312.
- [61] P. Wilczewska, A. Bielicka-Giełdoń, A.F. Borzyszkowska, J. Ryl, T. Klimczuk, E. M. Siedlecka, Photocatalytic activity of solvothermal prepared BiOClBr with imidazolium ionic liquids as a halogen sources in cytostatic drugs removal, *J. Photochem. Photobiol., A* 382 (2019) 111932–111943.
- [62] A. Wang, S. Guo, M. Xu, C. Meng, H. Zhu, T. Zheng, H. Wang, K. Wang, W. Shi, X. Liu, X. Song, Z. Chang, 0D/3D CNQDs/CuFe₂O₄/Cu⁰ heterostructures as broad spectrum photocatalyst for efficient 5-fluorouracil degradation: structural evolution and relay oxidation process, *Appl. Catal. B-Environ.* 322 (2023), 122117.